PNAS Nexus, 2024, 3, 1–12
https://doi.org/10.1093/pnasnexus/pgae001
Advance access publication 11 January 2024
Research Report

Human *RFX6* regulates endoderm patterning at the primitive gut tube stage

Toshihiro Nakamura[a], Junji Fujikura[a,*], Ryo Ito[a,b], Yamato Keidai[a] and Nobuya Inagaki[a,c,*]

[a]Department of Diabetes, Endocrinology and Nutrition, Graduate School of Medicine, Kyoto University, Kyoto 606-8507, Japan
[b]Center for iPS Cell Research and Application, Kyoto University, Kyoto 606-8507, Japan
[c]Medical Research Institute, Kitano Hospital, PIIF Tazuke-kofukai, Osaka 530-8480, Japan
*To whom correspondence should be addressed: Email: inagaki@kuhp.kyoto-u.ac.jp (N.I.); Email: jfuji@kuhp.kyoto-u.ac.jp (J.F.)
Edited By: J. Silvio Gutkind

Abstract

Transcriptional factor *RFX6* is known to be a causal gene of Mitchell–Riley syndrome (MRS), an autosomal recessive neonatal diabetes associated with pancreatic hypoplasia and intestinal atresia/malformation. The morphological defects are limited to posterior foregut and mid-hindgut endodermal lineages and do not occur in the anterior foregut lineage; the mechanism remains to be fully elucidated. In this study, we generated *RFX6*$^{+/eGFP}$ heterozygous knockin and *RFX6*$^{eGFP/eGFP}$ homozygous knockin/knockout human-induced pluripotent stem cell (hiPSC) lines and performed in vitro endoderm differentiation to clarify the role of RFX6 in early endoderm development. *RFX6* expression was found to surge at the primitive gut tube (PGT) stage in comparison with that in the undifferentiated or definitive endoderm stage. At the PGT stage, the expression of *PDX1* and *CDX2*, posterior foregut and mid-hindgut master regulators, respectively, was decreased by the RFX6 deficit. PDX1$^+$ and CDX2$^+$ cells were mostly green fluorescent protein (GFP)$^+$ in *RFX6*$^{+/eGFP}$ hiPSCs, but their cell number was markedly decreased in *RFX6*$^{eGFP/eGFP}$ hiPSCs. The expression of *SOX2*, an anterior foregut marker, was not affected by the RFX6 deficit. In addition, we found a putative RFX6-binding X-box motif using cap analysis of gene expression-seq and the motif-containing sequences in the enhancer regions of *PDX1* and *CDX2* bound to RFX6 in vitro. Thus, *RFX6* regulates the ParaHox genes *PDX1* and *CDX2* but does not affect *SOX2* in early endodermal differentiation, suggesting that defects in early stage endoderm patterning account for the morphological pathology of MRS.

Significance Statement

This study describes the role of human RFX6 in the early stage endoderm patterning that underlies the organogenetic disorders seen in Mitchell–Riley syndrome, a human RFX6-deficit disease with pancreatic hypoplasia and intestinal atresia/malformation presenting with neonatal diabetes and severe malnutrition. We demonstrate that *RFX6* regulates *PDX1* and *CDX2*, posterior foregut and mid-hindgut master transcriptional factors, respectively, but does not affect *SOX2*, an anterior foregut marker, at the primitive gut tube stage, by using in vitro endoderm differentiation of *RFX6*$^{+/eGFP}$ heterozygous knockin and *RFX6*$^{eGFP/eGFP}$ homozygous knockin/knockout human-induced pluripotent stem cell (hiPSC) reporter lines and nongene-modified hiPSCs. In addition, the *RFX6-eGFP* knockin hiPSC lines generated in this study may contribute to future pancreatic and intestinal endocrine research.

Introduction

The gene of human regulatory factor 6 (RFX6), a transcriptional factor composed of 928 amino acids, encoded by 19 exons on chromosome 6q22, was shown to be a regulatory factor X (RFX) family member (1, 2). *RFX6* was then identified as the causative gene of Mitchell–Riley syndrome (MRS; OMIM #615710) (3), which had been clinically recognized as an autosomal recessive disease characterized by endodermal organ dysgenesis including hypoplastic or annular pancreas with neonatal diabetes, intestinal atresia, and gallbladder hypoplasia or aplasia (4–6). Similar human cases with various mutations of *RFX6* were reported later (7–12); ectopic gastric tissue in the small intestine was observed in some cases (11, 12). The severity of the symptoms of MRS varies among patients but is often debilitating or fatal and includes severe malnutrition with diarrhea and high mortality in infancy. The pathological and clinical features of the disease suggest defects in the mechanism by which *RFX6* regulates tissue patterning and organogenesis of the endoderm.

Competing Interest: N.I. received clinical commissioned/joint research grants from Daiichi Sankyo, Terumo, and Drawbridge Inc.; speaker honoraria from Kowa, MSD, Astellas Pharma, Novo Nordisk Pharma, Ono Pharmaceutical, Nippon Boehringer Ingelheim, Takeda, Sumitomo Dainippon Pharma, and Mitsubishi Tanabe Pharma; and scholarship grants from Kissei Pharmaceutical, Sanofi, Daiichi Sankyo, Mitsubishi Tanabe Pharma, Takeda, Japan Tobacco, Kyowa Kirin, Sumitomo Dainippon Pharma, Astellas Pharma, MSD, Eli Lilly Japan, Ono Pharmaceutical, Sanwa Kagaku Kenkyu-sho, Nippon Boehringer Ingelheim, Novo Nordisk Pharma, Novartis Pharma, Teijin Pharma, and Life Scan Japan.
Received: June 9, 2023. **Accepted:** December 26, 2023

In regard to the role of *Rfx6* in the early developmental stage, a lineage-tracing mouse study revealed that the progeny cells of *Rfx6*-expressing cells were broadly observed in each endoderm lineage at embryonic day 10.5 but not in other lineages such as ectoderm and mesoderm (3). The study suggests that Rfx6 first appears in the earlier endoderm stage and expresses only in that lineage.

Compared with its broad distribution at the early endoderm stage, *RFX6* expression is restricted to the pancreas, small intestine, and colon, which are the posterior foregut and mid-hindgut-derived organs in human adults (13). Particularly in the pancreatic islet and intestinal enteroendocrine cell developmental stage, *Rfx6* is considered to be downstream of *Ngn3* (*Neurogenin 3*) and acts as the chief regulator of pancreatic and intestinal endocrine progenitor cell differentiation. *Ngn3* knockout mice show no *Rfx6* expression in the pancreatic islets (14). *NGN3*$^{-/-}$ and *RFX6*$^{-/-}$ human embryonic stem cells (hESCs) also exhibit very few C-peptide-positive cells in artificially differentiated islet-like cells, with almost no expression of *INS*, *GCG*, *SST*, or *GHRL* (15). Tamoxifen-induced *Villin-Cre Rfx6*$^{fl/fl}$, intestine-specific Rfx6 knockout mice, almost completely lack the expression of *Gcg*, *Ghrl*, *Gip*, *Pyy*, and *Cck* and partially lack Nts, Sst, and Sct in the intestine (16), while *Villin-Cre Ngn3*$^{fl/fl}$ mice lack all types of enteroendocrine cells (17). CRISPR-Cas9 mediated ex vivo *Rfx6*-knockout intestinal organoids of Rosa26-Cas9 mice show the reduction of *Gcg*, *Ghrl*, *Gip*, *Cck*, and *Tph1* expression, while *Ngn3* expression is not decreased (18).

However, congenital systemic RFX6 deficit results in more severe morphological disorders than NGN3 deficit. Unlike the severe disorganization of the pancreas and intestine found in MRS, loss-of-function mutation of human *NGN3* did not affect the upper gastrointestinal or small intestine follow-through and organ formation (19). *Rfx6*$^{-/-}$ mice exhibit hypogenesis of the pancreas and digestive tract disorders and therefore fail to feed normally, dying within 2 days postpartum (3), which is not the case in *Ngn3*$^{-/-}$ mice (20). The morphological discrepancy between the functional deficit of *RFX6* and *NGN3* suggests another *RFX6*-active phase in early endoderm development that controls the patterning of endodermal lineages differently from that of the *NGN3-RFX6* upstream–downstream relationship operant in the later pancreas and intestinal endocrine cell developmental stage.

This study focuses on the functional role of *RFX6* in the early stage of human endoderm patterning and development, which links the genetic features and the morphological disorders of MRS. We used human-induced pluripotent stem cells (hiPSCs), which enables us to recapitulate the early phase of human ontogeny with the least ethical limitations (21). In this study, we approach this unknown mechanism using in vitro endoderm differentiation of *RFX6*$^{+/+}$, *RFX6*$^{+/eGFP}$, and *RFX6*$^{eGFP/eGFP}$ *RFX6-eGFP* knockin hiPSC reporter lines that we generated.

Results

Generation of *RFX6*$^{+/eGFP}$ and *RFX6*$^{eGFP/eGFP}$ hiPSC lines

We first generated the *RFX6*$^{+/eGFP}$ heterozygous knockin and *RFX6*$^{eGFP/eGFP}$ homozygous knockout and knockin cell lines (Fig. 1a). In developing these cell lines, we performed homologous recombination using the bacterial artificial chromosome (BAC) with gene-modified human *RFX6*, in which an eGFP cassette is inserted just after the 5′ untranslated region (Fig. 1b). The specificity of the knockin locus was confirmed by fluorescent in situ hybridization (FISH) on the knockin reporter gene cassette. Signals of the inserted sequence were precisely identified in the decent target locus, chromosome 6q22, in one allele in *RFX6*$^{+/eGFP}$ and in both alleles in *RFX6*$^{eGFP/eGFP}$. Both cell lines maintain a normal karyotype identical to that in the parental line, 46 XX (Fig. 1c). The undifferentiated status of all cell lines was validated by alkaline phosphatase (ALP) activity and the undifferentiation markers, SSEA4, TRA-1-60, and NANOG (Fig. 1d). Pluripotency was confirmed by all three germ-layer markers, the ectoderm marker β3-Tubulin, the mesoderm marker α-smooth muscle actin (SMA), and the endoderm marker FOXA2, through in vitro differentiation after embryoid body (EB) formation (Fig. 1e and f). Each cell line survived well over 50 passages.

RFX6 is prominently expressed in the primitive gut tube stage

To determine the stage in which the *RFX6* expression surges, we differentiated the *RFX6*$^{+/+}$ hiPSC parental line to primitive gut tube (PGT) cells in vitro with a slight modification of the previous protocol (22), by which the cells were differentiated into the PGT stage through the definitive endoderm (DE) stage, expressing decent marker genes at each stage (Fig. 2a–d). *RFX6* expression was clearly increased at the PGT stage compared with that at the undifferentiated and DE stage (Fig. 2e). We then differentiated *RFX6*$^{+/eGFP}$ and *RFX6*$^{eGFP/eGFP}$ hiPSCs into the PGT stage by the same differentiation method to verify reporter gene expression. The general endoderm marker *FOXA2* expression was not altered in the three cell lines (Fig. 2f). *RFX6* expression decreased in an allele-dependent manner (Fig. 2g) and that of *eGFP* was detected only in knockin cell lines (Fig. 2h). We obtained similar results by western blotting (Fig. 2i). Immunocytochemistry images show that green fluorescent protein (GFP) was positive only for knockin cell lines and was negative for the parental cell line (Fig. 2j). Coimmunostaining of GFP and RFX6 of the *RFX6*$^{+/eGFP}$ hiPS line at the PGT stage (day 10) revealed similar signals of GFP and RFX6 but a relatively high nonspecific signal of anti-RFX6 antibody compared with that of anti-GFP antibody. Western blotting data support the immunocytochemistry data (Fig. S1).

Selection of candidate downstream genes of *RFX6*

To select candidate genes regulated by RFX6 during the DE stage to the PGT stage, we compared bulk gene expression between *RFX6*$^{+/+}$ and *RFX6*$^{eGFP/eGFP}$ hiPSCs at the PGT stage using the cap analysis of gene expression (CAGE)-seq. Among down-regulated genes in *RFX6*$^{eGFP/eGFP}$ hiPSCs, expression of the posterior foregut marker *PDX1* and the mid-hindgut marker *CDX2*, both of which are master transcriptional factors in the endoderm development, was detected (23). *NGN3*, which is thought to be upstream of *RFX6* in pancreatic endocrine cells, was also decreased at this stage (Fig. 2k and l).

PDX1 and *CDX2* expressing cells are decreased by the RFX6 deficit at the PGT stage

CDX2 expression was significantly up-regulated at the PGT stage compared with that of the predifferentiation and DE stage, similarly to *PDX1* (Figs. 2d and 3a). *RFX6* expression precedes *PDX1* and *CDX2* expression from the DE stage to the PGT stage (Fig. S2). Bulk expression of *PDX1* and *CDX2* at the PGT stage of *RFX6*$^{eGFP/eGFP}$ hiPSCs was decreased compared with that of *RFX6*$^{+/+}$ and *RFX6*$^{+/eGFP}$ hiPSCs (Fig. 3b and c). A flow cytometry analysis at this stage revealed that 97.1% of PDX1^{+} cells and 94.1% of CDX2^{+} cells were GFP^{+} in *RFX6*$^{+/eGFP}$ hiPSCs. The proportion of GFP^{+}PDX1^{+} cells in the GFP^{+} cells was 60.7% in *RFX6*$^{+/eGFP}$

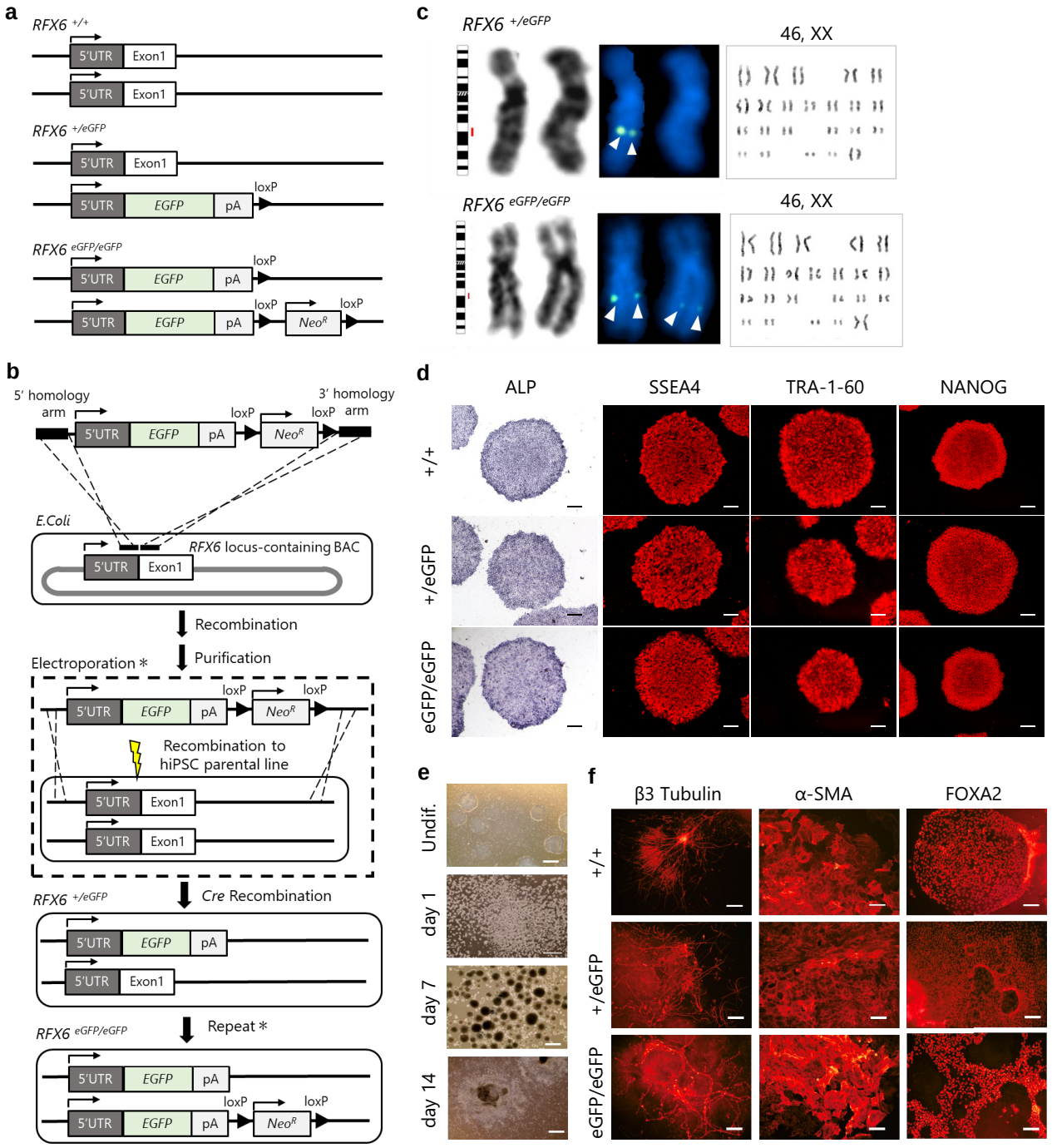

Fig. 1. The generation of *RFX6-eGFP* knockin cell lines. a) A schema of $RFX6^{+/+}$, $RFX6^{+/eGFP}$, and $RFX6^{eGFP/eGFP}$ hiPSCs. b) Schematic procedures to generate $RFX6^{+/eGFP}$ and $RFX6^{eGFP/eGFP}$ hiPSCs. c) A locus validation of $RFX6^{+/eGFP}$ and $RFX6^{eGFP/eGFP}$ hiPSCs by FISH. (Left) Ideogram and Q-banding images of chromosome 6. (Middle) FISH images of chromosome 6. The white triangles mark the signals of the inserted gene. (Right) Karyotype images. d) ALP activity and immunofluorescent images of SSEA4, TRA-1-60, and NANOG of the undifferentiated colony of $RFX6^{+/+}$, $RFX6^{+/eGFP}$, and $RFX6^{eGFP/eGFP}$ hiPSCs. Bar: 100 μm. e) Bright-field images of in vitro differentiation of EBs. Bar: 1 cm. f) Immunofluorescent images of the ectoderm marker β3-Tubulin, the mesoderm marker α-SMA, and the endoderm marker FOXA2 after in vitro EB differentiation of $RFX6^{+/+}$, $RFX6^{+/eGFP}$, and $RFX6^{eGFP/eGFP}$ hiPSCs. Bar: 100 μm.

hiPSCs, which decreased to 13.8% in $RFX6^{eGFP/eGFP}$; that of GFP^+CDX2^+ cells in GFP^+ cells was 76.0% in $RFX6^{+/eGFP}$ and 33.7% in $RFX6^{eGFP/eGFP}$ hiPSCs (Fig. 3d and e). Immunocytochemistry images indicated that GFP^+PDX1^+ cells were more predominantly observed than GFP^-PDX1^+ cells in $RFX6^{+/eGFP}$ hiPSCs, and the number of GFP^+PDX1^+ cells was decreased in $RFX6^{eGFP/eGFP}$ hiPSCs compared with that in $RFX6^{+/eGFP}$ hiPSCs, bolstering the results of the flow cytometry analysis (Fig. 3f). In regard to the PDX1 and CDX2 relationship, PDX1/CDX2 costaining shows that PDX1 and CDX2 are expressed simultaneously in some PGT cells in addition to $PDX1^+CDX2^-$ and $PDX1^-CDX2^+$ cells in $RFX6^{+/eGFP}$ hiPSCs, although the number of $PDX1^+CDX2^+$ cells was not as large as that of $PDX1^+CDX2^-$ and $PDX1^-CDX2^+$ cells (Fig. 3g). The number of $CDX2^+$ cells was decreased in $RFX6^{eGFP/eGFP}$ hiPSCs compared with that in $RFX6^{+/+}$ and $RFX6^{+/eGFP}$ hiPSCs (Fig. 3g). Multiple clones of $RFX6^{+/eGFP}$ and $RFX6^{eGFP/eGFP}$ hiPSC lines were assessed for *PDX1*

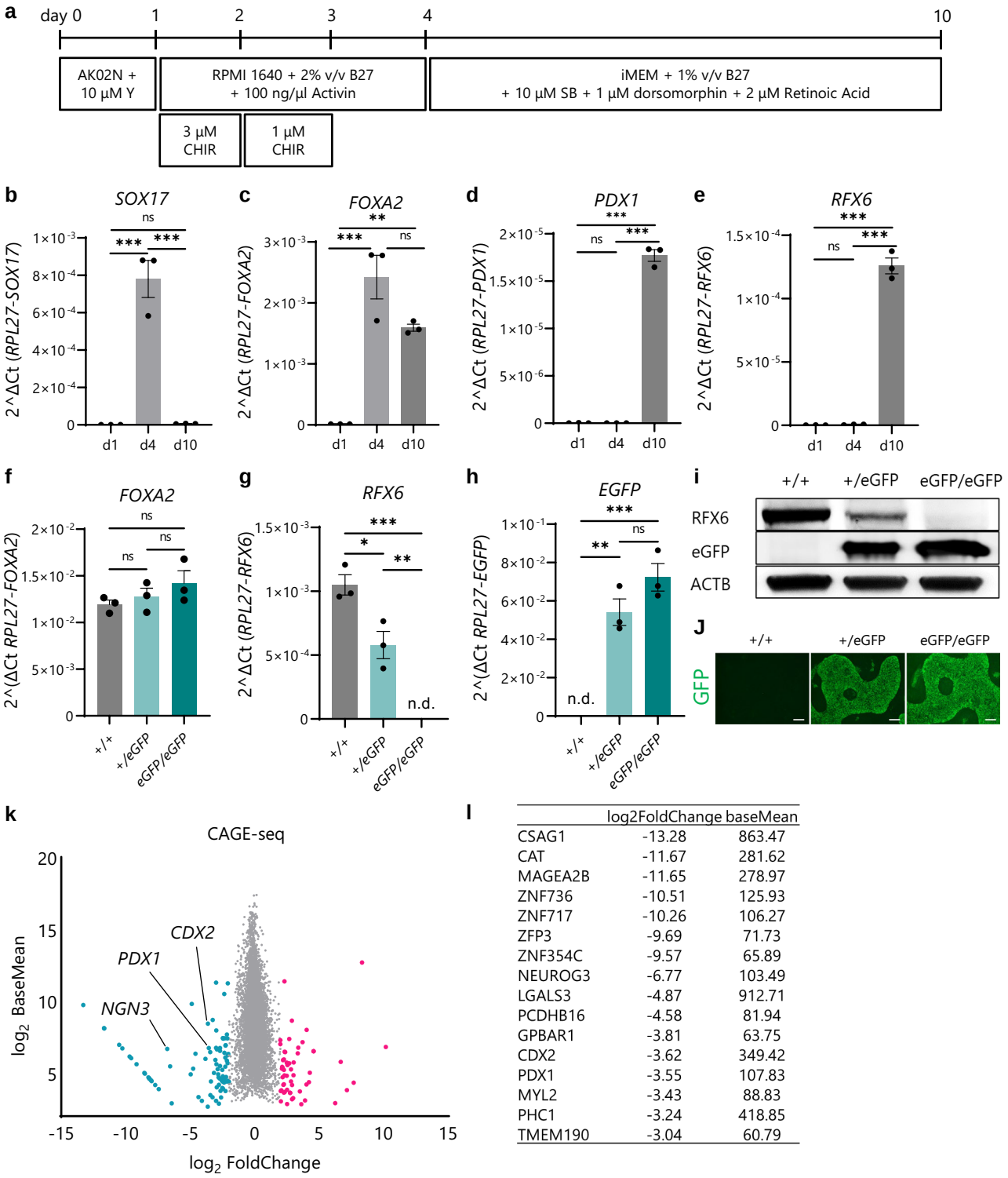

l

	log2FoldChange	baseMean
CSAG1	-13.28	863.47
CAT	-11.67	281.62
MAGEA2B	-11.65	278.97
ZNF736	-10.51	125.93
ZNF717	-10.26	106.27
ZFP3	-9.69	71.73
ZNF354C	-9.57	65.89
NEUROG3	-6.77	103.49
LGALS3	-4.87	912.71
PCDHB16	-4.58	81.94
GPBAR1	-3.81	63.75
CDX2	-3.62	349.42
PDX1	-3.55	107.83
MYL2	-3.43	88.83
PHC1	-3.24	418.85
TMEM190	-3.04	60.79

Fig. 2. *RFX6* expression during in vitro differentiation to the PGT stage, reporter gene validation, and RNA-seq to search candidate downstream genes of *RFX6*. a) In vitro differentiation method into the PGT stage (day 10) through the DE stage (day 4). b–e) Marker gene expression and *RFX6* expression of $RFX6^{+/+}$ with the qPCR at each in vitro differentiation stage. (Endogenous control is *RPL27*. $n = 3$. Bars are mean ± SD. ns, not significant. *<0.05, **<0.01, ***<0.001 for *P*-value.) f–h) *FOXA2*, *RFX6*, and reporter gene *EGFP* expression with the qPCR of $RFX6^{+/+}$, $RFX6^{+/eGFP}$, and $RFX6^{eGFP/eGFP}$ hiPSCs at the PGT stage. (Endogenous control is *RPL27*. $n = 3$. Bars are mean ± SD. n.d., not detected. ns, not significant. *<0.05, **<0.01, ***<0.001 for *P*-value.) i) Western blotting images of $RFX6^{+/+}$, $RFX6^{+/eGFP}$, and $RFX6^{eGFP/eGFP}$ hiPSCs at the PGT stage using ACTB as an endogenous control. j) GFP immunofluorescent images of $RFX6^{+/+}$, $RFX6^{+/eGFP}$, and $RFX6^{eGFP/eGFP}$ hiPSCs at the PGT stage. Bar: 100 μm. k) CAGE-seq gene plots comparing $RFX6^{+/+}$ hiPSCs with $RFX6^{eGFP/eGFP}$ hiPSCs at the PGT stage. The vertical line corresponds to fold change of the adjusted read number; the horizontal line correlates with the adjusted read number itself. The dots of down-regulated and up-regulated genes in $RFX6^{eGFP/eGFP}$ hiPSCs were highlighted respectively. l) A down-regulated gene list of $RFX6^{eGFP/eGFP}$ hiPSCs compared with $RFX6^{+/+}$ hiPSCs at the PGT stage.

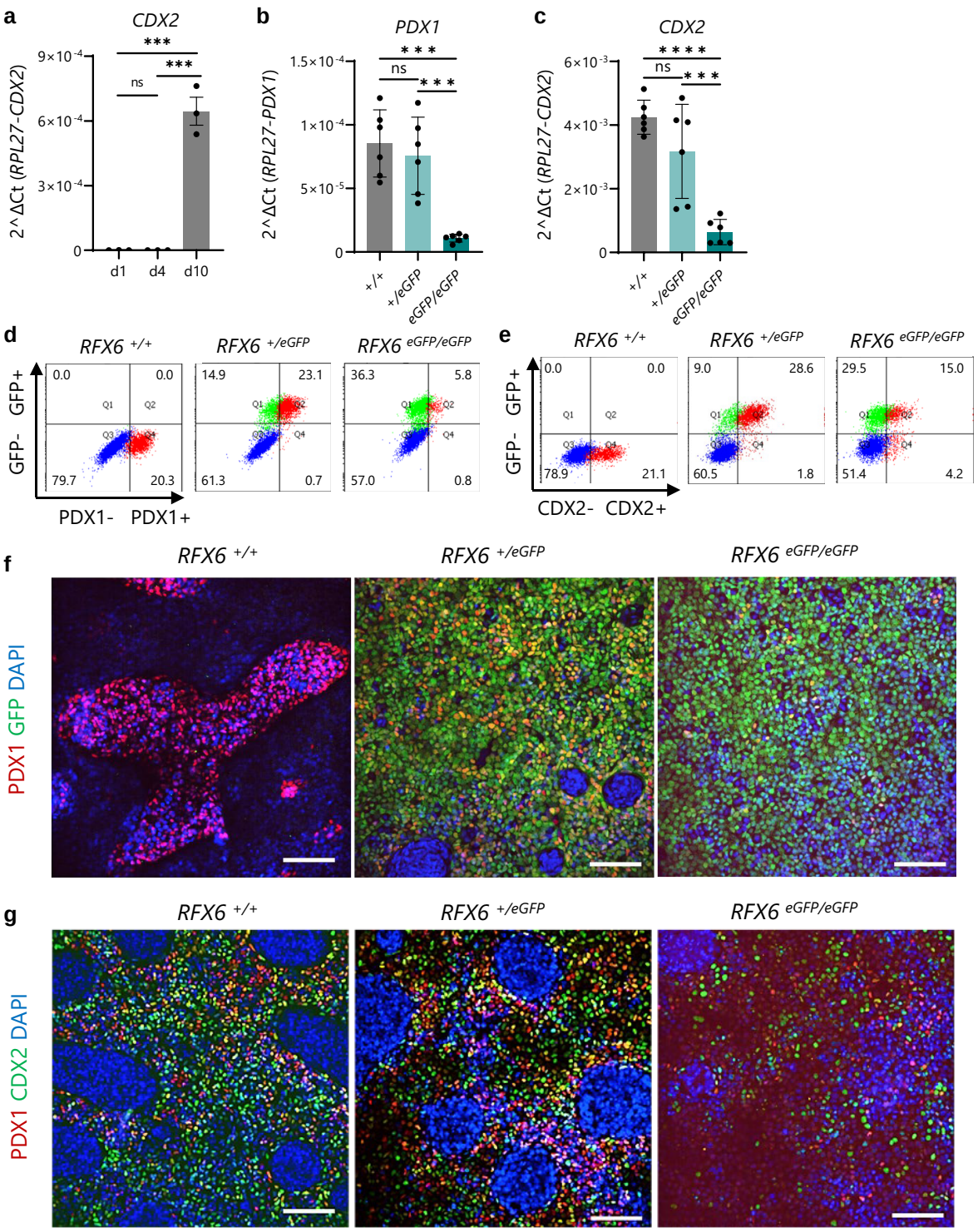

Fig. 3. *RFX6* regulates the posterior foregut marker *PDX1* and mid-hindgut marker *CDX2* at the PGT stage. a) *CDX2* expression of *RFX6*$^{+/+}$ hiPSCs at each in vitro differentiation stage ($n = 3$). b and c) *PDX1* and *CDX2* expression of *RFX6*$^{+/+}$, *RFX6*$^{+/eGFP}$, and *RFX6*$^{eGFP/eGFP}$ hiPSCs at the PGT stage. ($n = 6$. Endogenous control is *RPL27*. Bars are mean ± SD. ns, not significant. ***<0.001, ****<0.0001 for *P*-value.) d and e) A flow cytometry analysis of PDX1/GFP and CDX2/GFP at the PGT stage. GFP was unstained only with CDX2 due to antibody cross-activity. Most PDX1$^+$ and CDX2$^+$ cells are GFP$^+$, but PDX1$^+$GFP$^+$ and CDX2$^+$GFP$^+$ cell populations are reduced in *RFX6*$^{eGFP/eGFP}$ hiPSCs compared with those in *RFX6*$^{+/eGFP}$ hiPSCs. f and g) Immunofluorescent images of *RFX6*$^{+/+}$, *RFX6*$^{+/eGFP}$, and *RFX6*$^{eGFP/eGFP}$ hiPSCs at the PGT stage. Bar: 100 µm. f) PDX1 and GFP costaining images. In *RFX6*$^{+/eGFP}$ hiPSCs, PDX1$^+$GFP$^+$ cells are more dominant than PDX1$^+$GFP$^-$ cells. Such PDX1$^+$GFP$^+$ cells are sparse in *RFX6*$^{eGFP/eGFP}$ hiPSCs compared with the number in *RFX6*$^{+/eGFP}$ hiPSCs. g) PDX1 and CDX2 costaining images. Some PDX1$^+$CDX2$^+$ cells in addition to PDX1$^+$CDX2$^-$ and PDX1$^-$CDX2$^+$ cells are seen in *RFX6*$^{+/+}$ and *RFX6*$^{+/eGFP}$ hiPSCs. PDX1$^+$ and CDX2$^+$ cells are observed sporadically in *RFX6*$^{eGFP/eGFP}$ hiPSCs.

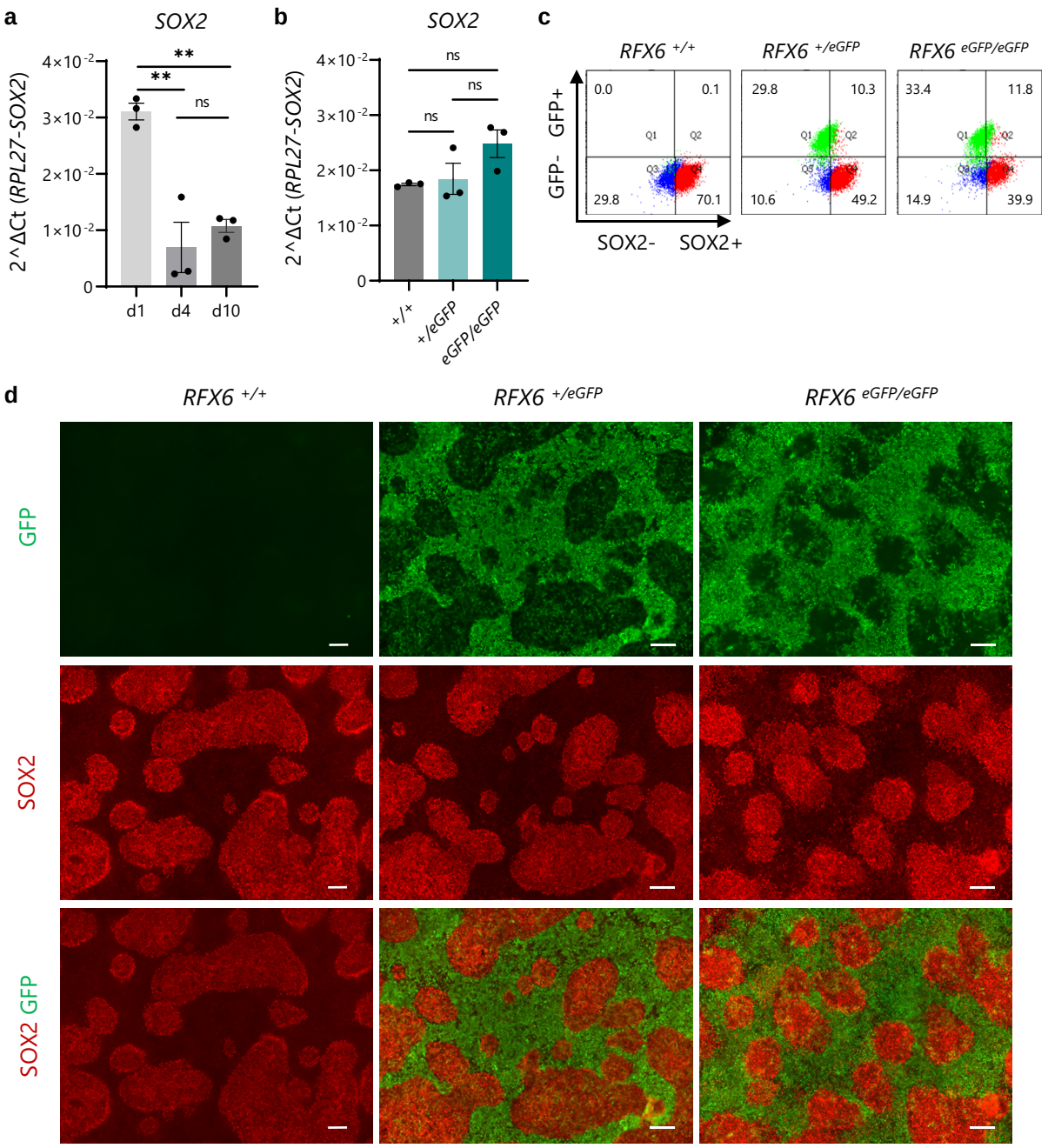

Fig. 4. *RFX6* does not down-regulate the anterior foregut marker *SOX2*. a) *SOX2* expression of *RFX6*$^{+/+}$ hiPSCs at each in vitro differentiation stage. b) *SOX2* expression of *RFX6*$^{+/+}$, *RFX6*$^{+/eGFP}$, and *RFX6*$^{eGFP/eGFP}$ hiPSCs at the PGT stage. (Endogenous control is *RPL27*. $n = 3$. Bars are mean ± SD. ns, not significant. **<0.01, ***<0.001 for *P*-value.) c) A flow cytometry analysis of SOX2/GFP at the PGT stage. Most SOX2^{+} cells are GFP^{-} and vice versa, in both *RFX6*$^{+/eGFP}$ and *RFX6*$^{eGFP/eGFP}$ hiPSCs. d) SOX2/GFP immunofluorescent images of *RFX6*$^{+/+}$, *RFX6*$^{+/eGFP}$, and *RFX6*$^{eGFP/eGFP}$ hiPSCs at the PGT stage.

and *CDX2* expression (Fig. S3). We compared another *PDX1*-prone differentiation protocol with the same differentiation duration (24). While *CDX2* expression remained relatively lower than the protocol used in this study, a similar decrease in *PDX1* and *CDX2* expressions due to the RFX6 deficit was nevertheless observed (Fig. S4).

The expression of *SOX2*, an anterior foregut marker, was not affected by the *RFX6* deficit

The expression of *SOX2*, which is known as an anterior foregut marker and an undifferentiation marker, was significantly decreased from the undifferentiation stage to the DE stage and tended to increase from DE to the PGT stage (Fig. 4a). At the PGT stage, *SOX2* expression did not differ among *RFX6*$^{+/+}$, *RFX6*$^{+/eGFP}$, and *RFX6*$^{eGFP/eGFP}$ hiPSCs (Fig. 4b). Flowcytometry analysis of SOX2 and GFP at the PGT stage indicated that the majority of SOX2^{+} cells were GFP^{-} in both *RFX6*$^{+/eGFP}$ and *RFX6*$^{eGFP/eGFP}$ hiPSCs (Fig. 4c). Immunocytochemistry images confirmed this finding (Fig. 4d).

A CATGGCAA X-box motif was detected using CAGE-seq as a target of RFX6

We also searched for a candidate RFX6-binding motif sequence by comparing GFP-positive cells of *RFX6*$^{+/eGFP}$ hiPSCs with those of *RFX6*$^{eGFP/eGFP}$ hiPSCs at the PGT stage by using CAGE-seq

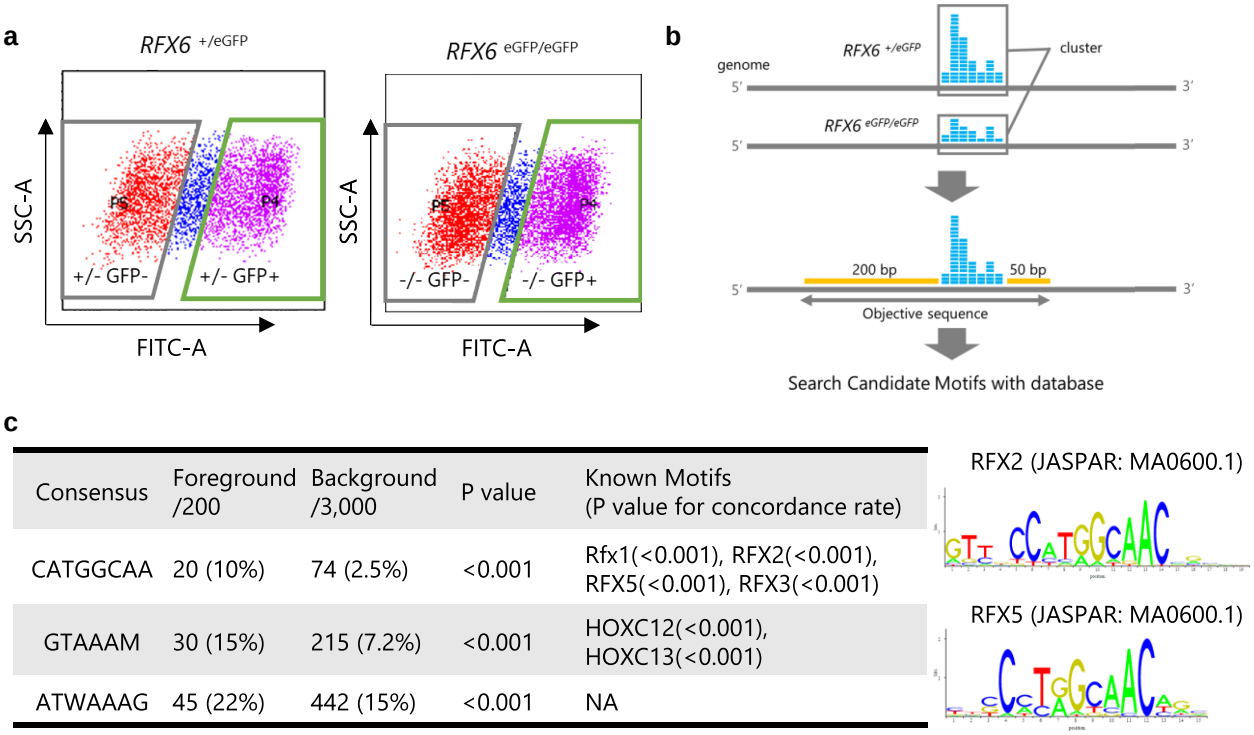

Consensus	Foreground /200	Background /3,000	P value	Known Motifs (P value for concordance rate)
CATGGCAA	20 (10%)	74 (2.5%)	<0.001	Rfx1(<0.001), RFX2(<0.001), RFX5(<0.001), RFX3(<0.001)
GTAAAM	30 (15%)	215 (7.2%)	<0.001	HOXC12(<0.001), HOXC13(<0.001)
ATWAAAG	45 (22%)	442 (15%)	<0.001	NA

Fig. 5. A RFX6-binding motif search. a) A living cell flow cytometry of *RFX6*$^{+/eGFP}$ and *RFX6*$^{eGFP/eGFP}$ hiPSCs at the PGT stage. GFP-positive, GFP-negative, and intermediate cells are highlighted separately. SSC-A, side scatter area; FITC-A, fluorescein isothiocyanate area. b) A schema of the motif search using CAGE-seq and motif databases. c) (left) Putative consensus motifs found by CAGE-seq and motif databases. Foreground objective sequences represent read clusters less frequently observed in *RFX6*$^{eGFP/eGFP}$ hiPSCs than in *RFX6*$^{+/eGFP}$ hiPSCs. Background sequences are those that did not show differences. Motif frequency in both foreground and background is also described as percentage. The *P*-value in the independent column denotes the difference in the frequency between foreground and background. The *P*-value in the parenthesis is calculated by using the concordance rate to the known motifs. (right) RFX2 and RFX5 ChIP-seq motif logos from the JASPAR database.

(Figs. 5a, b, and S5). By using motif databases, putative RFX6-binding motifs were surveyed in the sequencing read cluster in the range from 200 bp upstream to 50 bp downstream of the transcriptional starting site (TSS). The top 200 clusters down-regulated in *RFX6*$^{eGFP/eGFP}$ hiPSCs in comparison with *RFX6*$^{+/eGFP}$ hiPSCs were selected; the sequences of these clusters were compared with 3,000 random clusters that have no difference in both groups (Fig. 5b). Among the candidate motifs, we found a CATGGCAA motif that has not been reported previously as an RFX6-binding motif but is known to be an X-box motif of other RFX family members such as RFX2, RFX3, and RFX5 (Fig. 5c).

RFX6 binds to the CATGGCAA X-box site upstream of the *PDX1* and *CDX2* genes on the electrophoresis mobility shift assay

In the sequence of *PDX1* and *CDX2* genes, which are located closely at 13q12.2, the CATGGCAA motif was detected 10 kb upstream and 26 kb upstream of the TSS, respectively. The binding capacity of RFX6 to the motif was confirmed by electrophoresis mobility shift assay (EMSA) using a nonradioisotope method with biotin-end-labeled oligos. Purified RFX6 protein from HEK293-EF1α-*RFX6*-C-*Myc*-IRES-*Puro* transgenic cells was applied to EMSA. RFX6 protein bound to the labeled CATGGCAA-containing sequences found upstream of *PDX1* and *CDX2*; the binding was cancelled out by the excess nonbiotin-labeled probes (Fig. 6a). Signals of these bindings to each target sequence were not detected when the probe sequences lacked the CATGGCAA X-box (Fig. 6b).

Discussion

This study highlights the function of human RFX6 in the early endoderm developmental stage using *eGFP* reporter iPSC lines and provides clues to the relationship between the genetic and pathological features of MRS. The *RFX6* expression level is lower in the early developmental stages, making it more difficult to quantify its expression level with its antibody than it is in the adult/mature stage. Even so, *eGFP*, a highly sensitive reporter gene, permitted fine monitoring of the *RFX6* expression pattern, by which we found the clue to the pathophysiology of MRS: RFX6 positively affects PDX1 and CDX2 but not SOX2 at the PGT stage (Fig. 7).

Thus, the malformation of the pancreas and intestine, and severe diarrhea, the most frequent symptoms of MRS, can be ascribed to down-regulated *PDX1* and *CDX2* expression at the PGT stage, in which almost all PDX1$^+$ and CDX2$^+$ cells are RFX6$^+$ and the number of PDX1$^+$ cells and CDX2$^+$ cells is decreased by the RFX6 deficit. Pdx1 is the master regulator in pancreas organogenesis (25, 26) and also maintains gastroduodenal order in adults (27). Embryonic Cdx2 expression begins at E8.5 in the posterior gut (28); systemic Cdx2-null mice die around E3.5–5.5 (29) due to Cdx2 expression in the trophectoderm at E3.5 (28). *Villin-Cre/Cdx2*$^{fl/fl}$ intestinal Cdx2 knockout mice exhibit hypogenesis and loss of polarity of the small intestine at E18.5 (30). PDX1 and CDX2 were found to be partly coexpressed at the PGT stage in our study, as in a previous report alluding to a Pdx1$^+$/Cdx2$^+$ mixed region (27).

Contrary to the effect of the *RFX6* deficit on *PDX1* and *CDX2*, the deficit did not significantly affect the anterior foregut marker

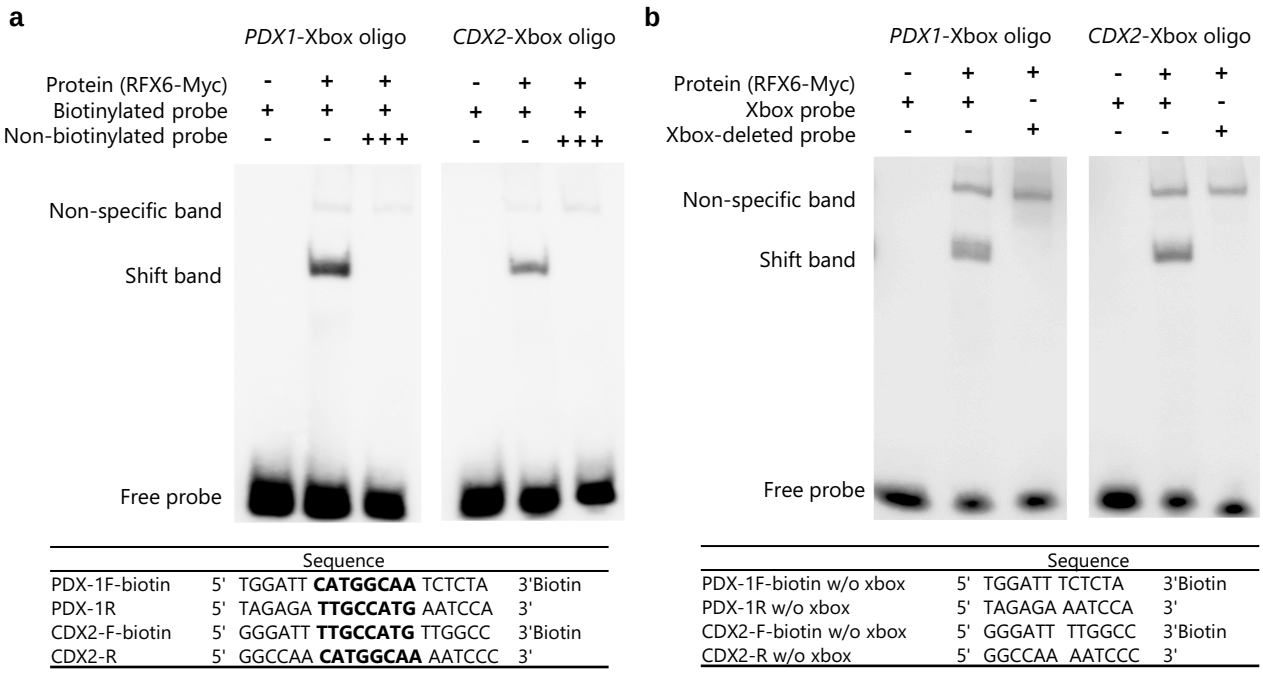

	Sequence		
PDX-1F-biotin	5'	TGGATT **CATGGCAA** TCTCTA	3'Biotin
PDX-1R	5'	TAGAGA **TTGCCATG** AATCCA	3'
CDX2-F-biotin	5'	GGGATT **TTGCCATG** TTGGCC	3'Biotin
CDX2-R	5'	GGCCAA **CATGGCAA** AATCCC	3'

	Sequence		
PDX-1F-biotin w/o xbox	5'	TGGATT TCTCTA	3'Biotin
PDX-1R w/o xbox	5'	TAGAGA AATCCA	3'
CDX2-F-biotin w/o xbox	5'	GGGATT TTGGCC	3'Biotin
CDX2-R w/o xbox	5'	GGCCAA AATCCC	3'

Fig. 6. RFX6 and putative X-box motif binding in a non-RI EMSA. a) EMSA images of the RFX6 protein and the *PDX1*-upstream or *CDX2*-upstream CATGGCAA motif sequence. The shift band diminishes by the excess amount of the nonbiotinylated probes. b) EMSA images comparing the binding capacity of the X-box-containing probe with the X-box-deleted probe to the RFX6 protein. The shift band is not detected with the X-box-deleted probe.

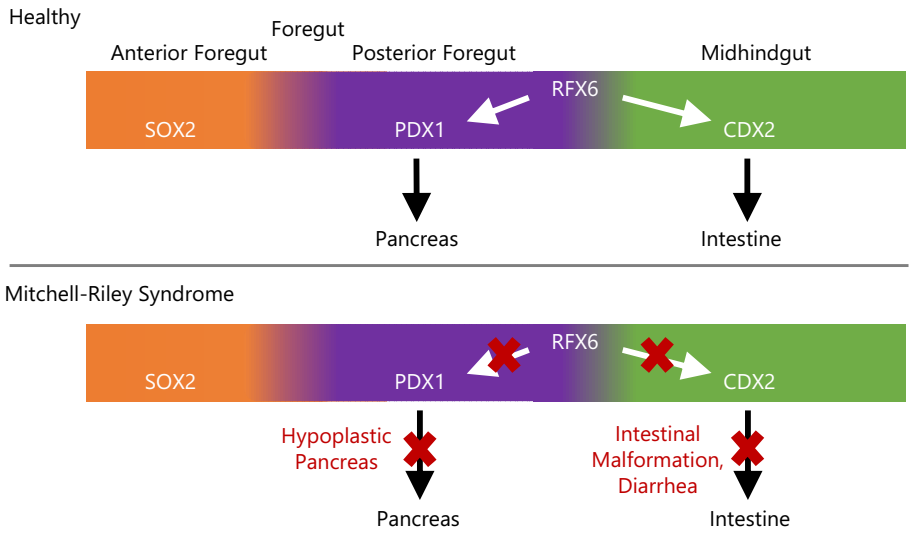

Fig. 7. The predicted pathophysiology of MRS. A schematic figure of the predicted pathophysiology of MRS. *RFX6* deficit causes *PDX1* and *CDX2* down-regulation, while not affecting *SOX2*. Patients with MRS, therefore, present with only the malformation of the posterior foregut–derived organs and mid-hind gut-derived organs but not the anterior foregut-derived organs.

SOX2. In regard to expression patterning at the PGT stage, interestingly, almost all of the differentiated cells at that stage were SOX2$^+$ or RFX6$^+$ and were distinctly segregated and complementary from each other, nearly all PDX1$^+$ cells and CDX2$^+$ cells being RFX6$^+$. Interestingly, ectopic gastric tissue in the small intestine, which is reported in some patients with MRS (11, 12), may be regarded as another consequence of the patterning disruption. It is known that the Pdx1 deficit results in anteriorization of the Pdx1-positive intestinal domain (27). Thus, the aberrant gastric tissue found in the small intestine of patients with MRS may well result from disruption by the RFX6 deficit, in which SOX2-dominant anterior foregut tube-prone tissue partially supplants the region destined by RFX6 to differentiate into posterior foregut and mid-hindgut-derived tissue. Meanwhile, possible change in the direction of differentiation toward gastric specification by the RFX6 deficit was not detected at the PGT stage in the comparison between *RFX6*$^{eGFP/eGFP}$ and *RFX6*$^{+/+}$ hiPSCs, nor was hepatic specification (Fig. S6). Gene expression alterations of histone acetyltransferase EP300, which has a promotive effect on liver development, and histone methyltransferase EZH2, which has a suppressive effect on pancreas development, were also not observed (31) (Fig. S6). Precise characterization will be a future consideration.

From a clinical viewpoint, ectopic gastric mucosa providing gastric acid secretion leads to pH changes in the small intestine and can cause diarrhea and intestinal ulcer. While only a few reports have surveyed the ectopic gastric mucosa, some of them have reported severe diarrhea and intestinal ulcer (11, 12) and, surprisingly, the resection of the ectopic gastric mucosa dramatically alleviates these symptoms in some cases (11). Thus, an intensive survey and a similar approach might be profitably applied in other MRS cases.

In regard to the direct binding of RFX6 to DNA, the CATGGCAA motif found in our study has been validated in several other members of the human RFX family, including RFX2, RFX3, and RFX5, although they do not have an entirely identical sequence of a DNA-binding domain (1). CCA(G/T)GT(C/T)(C/A)T, identified as the putative motif by the mouse ChIP assay using anti-mouse Rfx6 antibody (32), did not appear in our study sample. ChIP-validated RFX2 (MA0600.1) and RFX5 (MA0510.1) motifs have a robust frequency from −500 to +500 bp of the TSS within the range of −5,000 to +2,000 bp of the TSS (33), but it remains to be elucidated where these motifs are functional outside that range, including in the putative enhancer regions. The CATGGCAA motif, although not found in the *PDX1* and *CDX2* promoter regions, was found 10 kb upstream of the *PDX1* TSS and 26 kb upstream of the *CDX2* TSS and bound to RFX6. Interestingly, the *PDX1* and *CDX2* genes are located face-to-face on human chromosome 13. As similar functional gene positions are close to each other (34) and some adjacent genes share regulation mechanisms (35), the direct binding of RFX6 and the upstream X-box region of *PDX1/CDX2* genes suggests a possible function as an enhancer region.

The finding that the expression of *NGN3*, which is known as an upstream of *RFX6* in pancreatic endocrine cells, was decreased at the PGT stage further suggests the multiphasic role of *RFX6* in addition to the roles described in later developmental stages, including those as a developmental regulator in pancreatic islets and intestinal endocrine cells and a secretory regulator of mature pancreatic beta-cells (36). As the concept of multiphasic expression of transcriptional factors was reported previously (37), it is helpful to understand why the *NGN3-RFX6* upstream–downstream relationship in the later pancreatic and intestinal endocrine cell development and maturation stages cannot satisfactorily explain the morphological discrepancy between the *NGN3*-null and *RFX6*-null phenotypes.

Our *RFX6* iPSC reporter lines will contribute to future studies regarding the secretory machinery of pancreatic beta cells and enteroendocrine cells. Pancreatic-endocrine-specific *Rfx6*-deficiency mice show that *Rfx6* regulates genes that are involved in the insulin secretion (36); *RFX6*-knockdown of the human beta-cell line EndoC-βH2 (38) demonstrates the down-regulation of potassium channel genes (39). In addition, *Rfx6* up-regulates gastric inhibitory peptide (*GIP*) expression in enteroendocrine K cells in mice (40). It has also been found that some patients with maturity-onset diabetes of the young have an *RFX6* heterozygous-deficient genotype and present a decrease in both fasting and stimulated GIP secretion in the oral glucose tolerance test (41).

Additionally, among the up-regulated genes in the *RFX6* KO line (Fig. S6, related to Fig. 2k), *CPB1* encodes carboxypeptidase B1 and works specifically in pancreatic exocrine cells. *CPB1* up-regulation may reflect the inhibition of endocrine cell differentiation by RFX6 deficit. Although we mainly focused on the master regulator genes of the pancreas and intestine, influenced organs by the RFX6 deficit, such as *PDX1* and *CDX2* in this study, these functionally essential genes will be a promising target in future studies.

The findings of this study must be interpreted in consideration of some limitations. The disruption of endoderm regulation and patterning by the RFX6 deficit has not been validated in in vivo human *RFX6*-null embryo or fetus. Future studies are required to determine whether and how the boundary between $SOX2^+$ cells and $RFX6^+$ cells observed in the present study forms and what factors determine the boundary. In regard to *RFX6* regulation of *PDX1* and *CDX2*, although the binding of RFX6 and the CATGGCAA X-box was confirmed, it remains to be seen whether *RFX6* regulates them directly or indirectly.

Our findings indicate that human *RFX6* is essential in endoderm patterning at the PGT stage, regulating the posterior foregut marker *PDX1* and mid-hindgut marker *CDX2* but not the anterior foregut marker *SOX2*.

Methods

hiPSC parental line

hiPSC 409B2, a transgene- and virus-free iPSC generated from a Caucasian female, was used as a parental line (42).

Feeder-free hiPSC culture

About 60–70% confluent cells were detached with 0.5 mM ethylenediaminetetraacetic acid (EDTA)/phosphate-buffered saline (PBS) for 10 min at 37 °C. After adding AK02N (Ajinomoto) with 10 μM Y-27632 and centrifuging at 300×*g* for 5 min, the cells were seeded on iMatrix-511 silk (Nippi)-coated wells with AK02N with 10 μM Y-27632 with a split ratio of 1:200–1:500. Precoating and medium changes were performed according to the manufacturer's protocol.

Human *RFX6*-BAC recombineering

We used the homologous recombination method (43). First, a human *RFX6* BAC clone RP11-451L17 was transformed into *Escherichia coli* DH10B. Next, 50 bp 5′- and 3′-homology primer arms, identical sequences just before and after the first ATG of the human *RFX6* gene, were attached to the *eGFP-loxP-PGK-NeoR-loxP* cassette by PCR (98 °C 30 s, 30 cycles of 98 °C 10 s, 55 °C 30 s, and 72 °C 90 s, and 72 °C 10 min). Red/ET plasmid pSC101-BAD-gbaA was introduced to h*RFX6* BAC-containing *E. coli* by electroporation, and the knockin cassette was introduced by electroporation (2,500 V, 25 μF, and 200 Ω in 2 mm cuvette). After the G418 antibiotic selection and BAC purification, the recombination was confirmed by Sanger sequencing.

Generation of *RFX6*-GFP knockin hiPSC lines

A 30-μg knockin cassette-containing h*RFX6* BAC was linearized with PI-SceI and introduced to ~1.5×10^6 parental hiPSCs by electroporation. Cells were cultured in AK02N with 10 μM Y-27632 on day 0, AK02N without Y-27632 on day 1, and AK02N with 100 ng/μL G418 for about 2 weeks afterwards. We selected 15 candidate clones from 90 resistant clones by qPCR of genomic DNA.

Next, we removed the floxed *NeoR* lesion by transient Cre expression by using pHAGE2-EF1α-Cre-IRES-Puro (Addgene) (44). Approximately, 1×10^6 undifferentiated $RFX6^{+/eGFP\text{-}loxP\text{-}PGK\text{-}NeoR\text{-}loxP}$ cells were incubated with the mixture containing 90 μL Opti-MEM (Thermofisher) with 8 μL FuGENE HD (Promega) and 2 μg pHAGE2-EF1α-Cre-IRES-PuroR and then added to 6 mL AK02N with 10 μM Y-27632 and seeded on three wells of an iMatrix 511-silk precoated six-well plate. Cells were cultured in AK02N with 1 μg/mL Puromycin and without Y-27632 on the day after lipofection (day 1), and the medium changes were done with

AK02N without Puromycin and Y-27632 every other day from day 3. We picked up candidate colonies after 7–10 days. We selected the colony in which neither *NeoR* nor *Cre* was detected in genomic DNA as *RFX6*$^{+/eGFP\text{-}(NeoR\ deleted)}$ (*RFX6*$^{+/eGFP}$) hiPSCs. Finally, we repeated the same procedure of electroporation of the linearized BAC with the *RFX6*$^{+/eGFP\text{-}(NeoR\ deleted)}$ clone, G418 selection, and PCR confirmation and generated *RFX6*$^{eGFP\text{-}(NeoR\ deleted)/eGFP\text{-}loxP\text{-}PGK\text{-}NeoR\text{-}loxP}$ (*RFX6*$^{eGFP/eGFP}$) hiPSCs.

Q-banding karyotype and FISH

Q-banding karyotype analysis and FISH were performed at Chromosome Science Lab Inc. (Hokkaido, Japan). Q-banding analysis was performed on preparations processed with a Hoechst 33258 and quinacrine mustard double staining technique (45). For FISH, probe DNA plasmid, pBS II-EcoRV-*eGFP*-pA-PGK-*NeoR*-pA, generated from pBluescript II KS(-) (Agilent) was labeled with Cy3 by nick translation. After hybridization, stringency wash, and counterstaining with DAPI, the probe signal was detected on a Leica CW-4000 cytogenetic workstation.

Immunofluorescent staining

Cells were fixed with 4% paraformaldehyde. Except for SSEA4, cells were permeabilized with 100% ethanol at −20 °C for 10 min. After washing with PBS three times and blocking with Protein Block Serum-Free (PBSF, Dako/Agilent) at room temperature for 1 h, primary antibodies with PBSF were applied at 4 °C overnight. After washing with PBS three times, secondary antibodies with PBSF were applied at room temperature for 1 h. After washing with PBS three times, the cells were mounted with 5× PBS-diluted DAPI-Fluoromount G (SouthernBiotech). Fluorescence microscope images were captured with BZ-X710 (KEYENCE) or Dragonfly (Andor/Oxford Instruments). Antibodies are listed in Table S2.

ALP activity staining

BCIP/NBT Substrate System (Dako) was used according to the manufacturer's instruction.

EB formation and in vitro trilineage differentiation

Undifferentiated hiPSC colonies were detached and applied to the floating culture with AK02N with 10 μM Y-276342 on day 0 and with only AK02N afterwards. After sphere-shaped EB formation and expansion for 5–7 days, EBs were put on the gelatin-coated dish for the following week and harvested with DMEM with 10% FBS to form trilineage cells spontaneously. Trilineage differentiation was confirmed by immunocytochemistry of the ectoderm marker β3-Tubulin, the mesoderm marker α-SMA, and the endoderm marker FOXA2.

Differentiation from hiPSC to PGT cells

Subconfluent hiPS colonies were detached, and 200,000 iPS cells/well were seeded on the iMatrix-precoated well of a 24-well plate with 1 mL AK02N with 10 μM Y-276342 on day 0. Cells were cultured with 1 mL RPMI1640 with 2% vol/vol B27 supplement, 100 ng/mL activin A (DE basal medium), and 3 μM CHIR99021 on day 1, DE basal medium with 1 μM CHIR99021 on day 2, and DE basal medium only on day 3 followed by 1 mL improved MEM Zinc Option medium with 1% B27, 1 μM dorsomorphin, 2 μM retinoic acid, and 10 μM SB431542 on days 4, 6, and 8. Medium changes were made every 24 ± 2 h until day 4 and every 48 ± 2 h afterwards. We also used another *PDX1*-prone differentiation protocol to validate the consistency of the major results (Fig. S4) (24).

RNA extraction and qPCR

We used RNA-easy Kit, QIAshredder, and RNase-Free DNase Set (Qiagen, USA) for RNA extraction, ReverTra Ace qPCR RT Kit (Toyobo, Japan) for reverse transcription, and Thunderbird SYBR qPCR Mix for qPCR (Toyobo), according to the manufacturer's protocols. The amount of cDNA used for qPCR was equivalent to 40 ng total RNA. qPCR was performed at 95 °C for 10 min and 40 cycles at 95 °C for 15 s and at 60 °C for 60 s on StepOne Plus (Applied Biosystems, USA). $2^{\Delta Ct}$ value was used in the data analysis. Primers are listed in Table S1.

Flow cytometry

For immunofluorescent staining, detached cells were pipetted with fixation/permeabilization solution (BD) in the ratio of 1 μL/1 × 10^4 cells and incubated at room temperature for 30 min. After centrifuging at 300×*g* for 5 min, pellet cells were mixed with 2% donkey serum (DS) in 1× perm/wash (PW) buffer (BD) in the ratio of 1 mL/2 × 10^6 cells and stored at 4 °C. Fifty microliters of the mixture were applied onto the 96-well plate. After centrifuging at 400×*g* for 3 min (*), pellet cells and the primary antibody diluted with 100 μL 2% DS-PW were mixed at 4 °C overnight. After repeating (*), pellet cells were washed with PW buffer twice. Pellet cells and secondary antibodies diluted with 100 μL 2% DS-PW were mixed at room temperature for 1 h. After washing with PW buffer twice, the cells were sorted by FACS Aria 2 (BD). In flow cytometry of CDX2 and GFP, CDX2 was stained and GFP was unstained. Antibodies are listed in Table S2.

Cap analysis of gene expression-seq

CAGE library preparation, sequencing, mapping, gene expression, and motif discovery analysis were performed by DNAFORM (Kanagawa, Japan). cDNA was synthesized from total RNA using random primers. Ribose diols in the 5′-cap structures of RNA were oxidized and biotinylated. The biotinylated RNA/cDNAs were selected by streptavidin beads after RNase digestion. After an adaptor ligation to both cDNA ends, double-stranded cDNA libraries were sequenced using single-end 75-nucleotide reads on a NextSeq 500 instrument (Illumina). CAGE-tag reads were mapped to the RefSeq GRCh38 using BWA (ver. 0.5.9). Unmapped reads were mapped by HISAT 2 (ver. 2.0.5). For the bulk CAGE experiment, CAGE-tag clustering and analysis were performed by CAGEr (46). Genes with Log_2-fold change below −2.0 or above +2.0 and base means above 50 are listed, and WebGestalt2019 was used for overrepresentation analysis for these gene lists (47). For motif analysis experiment, pipeline RECLU (48) was used. In this procedure, genomic DNA sequences from 200 bp upstream to 50 bp downstream of differentially expressed CAGE peaks were subjected to de novo motif discovery tools.

Western blotting

Fifty milligrams of whole lysate protein were extracted with radioimmunoprecipitation assay (RIPA) Buffer with 1% Protease Inhibitor (Nacalai). The concentration was calculated by Protein Assay BCA kit (Nacalai). Samples were treated with 6× Sample Buffer Solution with 2-ME at 95 °C for 5 min. Electrophoresis was performed using Criterion Cell, Criterion Blotter, Criterion XT Precast Gel (Bio-Rad), and Immobilon-P PVDF membrane (Merck). Protein separation was carried out at 200 V for 1 h with a 20× DW-diluted XT MOPS Running Buffer (Bio-Rad). Membrane transfer was performed at 120 V for 1 h with the transfer buffer (25 mM Tris-HCl, 192 mM Glycine, and 10% Methanol in DW). We used 4% Block Ace (UKB) diluted with PBS for blocking at

room temperature for 1 h. After 2× wash with PBS for 10 min, the primary antibody was applied overnight at 4 °C. Then, after 2× wash with 0.2% Block Ace with PBS (PBS-B) for 10 min, the secondary antibody was applied for 1 h at room temperature. After 4× wash with 0.1% Tween 20 with PBS-B, chemiluminescence reaction was performed using Chemi-Lumi One Super (Nacalai). Blocking, washing, and antibody reactions were done on a plate shaker. Image capture was performed with ImageQuant LAS-4000 mini (GE Healthcare/Cytiva). Antibodies are listed in Table S2.

Electrophoresis mobility shift assay

For protein extraction, HEK293-EF1α-RFX6-Myc-DDK-IRES-Puro overexpression cells were generated by transfection of pLenti-EF1α-hRFX6ORF-Myc-DDK-IRES-Puro (OriGene) to HEK293 cells. Confluent cells of a 10-cm culture plate were detached with 0.25% Trypsin/EDTA and precipitated by centrifuge. After the PBS wash, pellet cells were treated with 500 µL M-PER Mammalian Protein Extraction Reagent (Thermofisher) with 1% Protease Inhibitor. The lysate was purified using c-Myc tagged Protein MILD PURIFICATION KIT ver. 2 (MBL) according to the manufacturer's protocol with slight modification in the rotation time of the beads-lysate mixture from 1 h to overnight. The purified protein concentration was ~0.5–1 µg/µL. Oligonucleotide probes for EMSA were dissolved with TEN Buffer (10 mM Tris; pH 8.0, 1 mM EDTA, and 0.1 mM NaCl) and annealed in a 1:1 sense–antisense ratio using natural cooling to room temperature after treatment at 94 °C for 10 min.

Protein size separation was performed using Mini-PROTEAN Tetra Cell, 5% Mini-PROTEAN TBE Precast Gel (Bio-Rad), and 1×Tris-borate EDTA (TBE) Buffer. In a 20-µL assay sample, 1.25 µg protein, 40 fmol biotinylated probe, 0–8 pmol nonbiotinylated probe, 2 µL 10× Binding Buffer (100 mM Tris, 500 mM KCl, 10 mM DTT; pH 7.5), 3 µL 50% glycerol, 1 µL 60 mM $MgCl_2$, 1 µL 10 mM EDTA, and DW up to 20 µL were used. After the prerun at 100 V for 45 min and concurrent protein–probe reaction at 25 °C for 20 min, 20 µL of the sample mixture with 2 µL 5× Nucleic Acid Sample Loading Buffer (Bio-Rad) was electrophoresed at 100 V for 35 min. Membrane transfer was performed using Trans-Blot Turbo, Zeta-Probe Blotting Membranes (Bio-Rad), and 0.5× TBE Buffer. After equilibration with 0.5× TBE for 10 min, transfer was performed at 0.2 A for 1 h. DNA crosslink to the membrane was performed at 120 mJ/cm^2 with UV Crosslinker, CL-1000 (UVP). Signal detection of biotin-labeled probes was performed with Chemiluminescent Nucleic Acid Detection Module Kit (Thermofisher). Images were captured with ImageQuant LAS-4000 mini (GE Healthcare/Cytiva).

Data analysis

All comparative analyses for qPCR were performed with one-way ANOVA followed by Tukey's multiple comparison test using GraphPad Prism ver. 9.5.1 (GraphPad Software). *P*-value <0.05 was regarded as statistically significant.

Acknowledgments

The authors thank Sara Yasui, Saki Kanda, Ayaka Shiota, and Yoshie Fukuchi for their laboratory assistance. The authors also thank the Medical Research Support Center, Graduate School of Medicine, Kyoto University, for using their research facility.

Supplementary Material

Supplementary material is available at *PNAS Nexus* online.

Funding

This study was supported by the Japan Society for the Promotion of Science (JSPS KAKENHI grant numbers 21K06970 and 22K08668), the Japan Foundation for Applied Enzymology (Front Runner of Future Diabetes Research), the Foundation of Future Research Support and the Japan Agency for Medical Research and Development (JP23ym0126125). The authors also acknowledge the support of the Japan Association for Diabetes Education and Care through an international travel grant.

Author Contributions

T.N. contributed to the study conception, researched the data, and wrote the manuscript. J.F. contributed to the study conception, researched the data, and revised the manuscript. R.I. researched the data and contributed to the discussion. Y.K. researched the data and contributed to the discussion. N.I. organized the study and contributed to the discussion.

Data Availability

The data that support the findings of this study are available in the supplementary material.

Ethical Approval

This study was approved by the Ethics Committee of Kyoto University Graduate School and Faculty of Medicine and Kyoto University Hospital (R0091).

References

1 Aftab S, Semenec L, Chu JS, Chen N. 2008. Identification and characterization of novel human tissue-specific RFX transcription factors. *BMC Evol Biol*. 8:226.
2 Emery P, Durand B, Mach B, Reith W. 1996. RFX proteins, a novel family of DNA binding proteins conserved in the eukaryotic kingdom. *Nucleic Acids Res*. 24:803–807.
3 Smith SB, *et al.* 2010. Rfx6 directs islet formation and insulin production in mice and humans. *Nature*. 463:775–780.
4 Mitchell J, *et al.* 2004. Neonatal diabetes, with hypoplastic pancreas, intestinal atresia and gall bladder hypoplasia: search for the aetiology of a new autosomal recessive syndrome. *Diabetologia*. 47:2160–2167.
5 Chappell L, *et al.* 2008. A further example of a distinctive autosomal recessive syndrome comprising neonatal diabetes mellitus, intestinal atresias and gall bladder agenesis. *Am J Med Genet Part A*. 146:1713–1717.
6 Martinovici D, *et al.* 2010. Neonatal hemochromatosis and Martinez-Frias syndrome of intestinal atresia and diabetes mellitus in a consanguineous newborn. *Eur J Med Genet*. 53:25–28.
7 Spiegel R, *et al.* 2011. Clinical characterization of a newly described neonatal diabetes syndrome caused by RFX6 mutations. *Am J Med Genet Part A*. 155:2821–2825.
8 Concepcion JP, *et al.* 2014. Neonatal diabetes, gallbladder agenesis, duodenal atresia, and intestinal malrotation caused by a novel homozygous mutation in RFX6. *Pediatr Diabetes*. 15: 67–72.

9 Khan N, Dandan W, Al Hassani N, Hadi S. 2016. A newly-discovered mutation in the RFX6 gene of the rare Mitchell-Riley syndrome. *J Clin Res Pediatr Endocrinol*. 8:246–249.

10 Zegre Amorim M, *et al.* 2015. Mitchell-Riley syndrome: a novel mutation in RFX6 gene. *Case Rep Genet*. 2015:937201.

11 Skopkova M, *et al.* 2016. Two novel RFX6 variants in siblings with Mitchell-Riley syndrome with later diabetes onset and heterotopic gastric mucosa. *Eur J Med Genet*. 59:429–435.

12 Sansbury FH, *et al.* 2015. Biallelic RFX6 mutations can cause childhood as well as neonatal onset diabetes mellitus. *Eur J Hum Genet*. 23:1744–1748.

13 Pearl EJ, Jarikji Z, Horb ME. 2011. Functional analysis of Rfx6 and mutant variants associated with neonatal diabetes. *Dev Biol*. 351: 135–145.

14 Soyer J, *et al.* 2010. Rfx6 is an Ngn3-dependent winged helix transcription factor required for pancreatic islet cell development. *Development*. 137:203–212.

15 Zhu Z, *et al.* 2016. Genome editing of lineage determinants in human pluripotent stem cells reveals mechanisms of pancreatic development and diabetes. *Cell Stem Cell*. 18:755–768.

16 Piccand J, *et al.* 2019. Rfx6 promotes the differentiation of peptide-secreting enteroendocrine cells while repressing genetic programs controlling serotonin production. *Mol Metab*. 29:24–39.

17 Mellitzer G, *et al.* 2010. Loss of enteroendocrine cells in mice alters lipid absorption and glucose homeostasis and impairs postnatal survival. *J Clin Invest*. 120:1708–1721.

18 Gehart H, *et al.* 2019. Identification of enteroendocrine regulators by real-time single-cell differentiation mapping. *Cell*. 176: 1158–1173.e16.

19 Wang J, *et al.* 2006. Mutant neurogenin-3 in congenital malabsorptive diarrhea. *N Engl J Med*. 355:270–280.

20 Gradwohl G, Dierich A, LeMeur M, Guillemot F. 2000. Neurogenin3 is required for the development of the four endocrine cell lineages of the pancreas. *Proc Natl Acad Sci U S A*. 97: 1607–1611.

21 Takahashi K, *et al.* 2007. Induction of pluripotent stem cells from adult human fibroblasts by defined factors. *Cell*. 131:861–872.

22 Kunisada Y, Tsubooka-Yamazoe N, Shoji M, Hosoya M. 2012. Small molecules induce efficient differentiation into insulin-producing cells from human induced pluripotent stem cells. *Stem Cell Res*. 8:274–284.

23 Mcgrath PS, Wells JM. 2015. SnapShot: GI tract development. *Cell*. 161:176.e1.

24 Ito R, *et al.* 2023. Elucidation of HHEX in pancreatic endoderm differentiation using a human iPSC differentiation model. *Sci Rep*. 13:8659.

25 Jonsson J, Carlsson L, Edlund T, Edlund H. 1994. Insulin-promoter-factor 1 is required for pancreas development in mice. *Nature*. 371:606–609.

26 Offield MF, *et al.* 1996. PDX-1 is required for pancreatic outgrowth and differentiation of the rostral duodenum. *Development*. 122: 983–995.

27 Holland AM, Garcia S, Naselli G, Macdonald RJ, Harrison LC. 2013. The parahox gene Pdx1 is required to maintain positional identity in the adult foregut. *Int J Dev Biol*. 57:391–398.

28 Beck F, Erler T, Russell A, James R. 1995. Expression of Cdx-2 in the mouse embryo and placenta: possible role in patterning of the extra-embryonic membranes. *Dev Dyn*. 204:219–227.

29 Chawengsaksophak K, James R, Hammond VE, Köntgen F, Beck F. 1997. Homeosis and intestinal tumours in Cdx2 mutant mice. *Nature*. 386:84–87.

30 Grainger S, Savory JGA, Lohnes D. 2010. Cdx2 regulates patterning of the intestinal epithelium. *Dev Biol*. 339:155–165.

31 Xu CR, *et al.* 2011. Chromatin "prepattern" and histone modifiers in a fate choice for liver and pancreas. *Science*. 332:963–966.

32 Cheng C, *et al.* 2019. Identification of Rfx6 target genes involved in pancreas development and insulin translation by ChIP-seq. *Biochem Biophys Res Commun*. 508:556–562.

33 Sugiaman-Trapman D, *et al.* 2018. Characterization of the human RFX transcription factor family by regulatory and target gene analysis. *BMC Genomics*. 19:181.

34 Thévenin A, Ein-Dor L, Ozery-Flato M, Shamir R. 2014. Functional gene groups are concentrated within chromosomes, among chromosomes and in the nuclear space of the human genome. *Nucleic Acids Res*. 42:9854–9861.

35 Imai KS, Daido Y, Kusakabe TG, Satou Y. 2012. Cis-acting transcriptional repression establishes a sharp boundary in chordate embryos. *Science*. 337:964–967.

36 Piccand J, *et al.* 2014. Rfx6 maintains the functional identity of adult pancreatic β cells. *Cell Rep*. 9:2219–2232.

37 Villasenor A, Chong DC, Cleaver O. 2008. Biphasic Ngn3 expression in the developing pancreas. *Dev Dyn*. 237:3270–3279.

38 Scharfmann R, *et al.* 2014. Development of a conditionally immortalized human pancreatic β cell line. *J Clin Invest*. 124: 2087–2098.

39 Chandra V, *et al.* 2014. RFX6 regulates insulin secretion by modulating Ca^{2+} homeostasis in human β cells. *Cell Rep*. 9:2206–2218.

40 Suzuki K, *et al.* 2013. Transcriptional regulatory factor X6 (RFX6) increases gastric inhibitory polypeptide (GIP) expression in enteroendocrine k-cells and is involved in GIP hypersecretion in high fat diet-induced obesity. *J Biol Chem*. 288:1929–1938.

41 Patel KA, *et al.* 2017. Heterozygous RFX6 protein truncating variants are associated with MODY with reduced penetrance. *Nat Commun*. 8:888.

42 Okita K, *et al.* 2011. A more efficient method to generate integration-free human iPS cells. *Nat Methods*. 8:409–412.

43 Mae S-I, *et al.* 2013. Monitoring and robust induction of nephrogenic intermediate mesoderm from human pluripotent stem cells. *Nat Commun*. 4:1367.

44 Somers A, *et al.* 2010. Generation of transgene-free lung disease-specific human induced pluripotent stem cells using a single excisable lentiviral stem cell cassette. *Stem Cells*. 28: 1728–1740.

45 Yoshida MC, Ikeuchi T, Sasaki M. 1975. Differential staining of parental chromosomes in interspecific cell hybrids with a combined quinacrine and 33258 Hoechst technique. *Proc Jpn Acad*. 51:184–187.

46 Haberle V, Forrest AR, Hayashizaki Y, Carninci P, Lenhard B. 2015. CAGEr: precise TSS data retrieval and high-resolution promoterome mining for integrative analyses. *Nucleic Acids Res*. 43: e51.

47 Liao Y, Wang J, Jaehnig EJ, Shi Z, Zhang B. 2019. WebGestalt 2019: gene set analysis toolkit with revamped UIs and APIs. *Nucleic Acids Res*. 47:W199–W205.

48 Ohmiya H, *et al.* 2014. RECLU: a pipeline to discover reproducible transcriptional start sites and their alternative regulation using capped analysis of gene expression (CAGE). *BMC Genomics*. 15: 1–15.